Applied Catalysis B: Environmental 322 (2023) 122130

Contents lists available at ScienceDirect

Applied Catalysis B: Environmental

journal homepage: www.elsevier.com/locate/apcatb

Interfacial electric field triggered N_2 activation for efficient electrochemical synthesis of ammonia

Xiaoxuan Wang, Xinyue Chi, Zhenzhen Fu, Yuanyuan Xiong, Shuyuan Li, Yebo Yao, Kaixin Zhang, Yongjia Li, Shiyu Wang, Rui Zhao, Zhiyu Yang, Yi-Ming Yan *

State Key Lab of Organic–Inorganic Composites, Beijing Advanced Innovation Center for Soft Matter Science and Engineering, Beijing University of Chemical Technology, Beijing 100029, People's Republic of China

ARTICLE INFO

Keywords:
Electrochemical nitrogen reduction
Interfacial electric field
CoO-Co_3O_4 heterostructure
N_2 adsorption and activation
N_2 distortion and polarization

ABSTRACT

Electrochemical nitrogen reduction reaction (ENRR) is a sustainable approach to producing carbon-free ammonia under ambient conditions, while its performance has been severely limited by the poor activity of electrocatalysts. Here, we report the deliberate modulation of interfacial electric field at the CoO-Co_3O_4 interface as an effective strategy for boosting ENRR performance. The prepared CoO-Co_3O_4 showed a promising NH_3 yield of 59.96 μg h^{-1} mg_{cat}^{-1} and high Faradaic efficiency (FE) of 22.37 % in 0.1 M Li_2SO_4. In situ Raman spectroscopy, in situ Fourier transform infrared (FTIR) spectra and theoretical calculations demonstrated that the engineered strong interfacial electric field in CoO-Co_3O_4 electrocatalyst act synergistically to capture inert N_2 by forming strong Co-N bonds. Subsequently, the interfacial electric field enhanced σ-d orbital hybridization between N_2 molecule and Co site of CoO-Co_3O_4, achieving highly efficient N_2 molecule activation. This work provides a deep understanding of electric field effect on the performance of ENRR catalysts.

1. Introduction

Ammonia (NH_3), a green fuel and high-energy density hydrogen carrier, plays a significant role in modern agriculture[1]. The traditional industrial synthesis of ammonia relies on Haber-Bosch process, which requires high temperatures and high pressures, leading to huge energy consumption and an enormous carbon footprint [2–7]. Alternatively, electrochemical nitrogen reaction reduction (ENRR) has been considered as a promising technology for producing NH_3 under ambient conditions [8–13]. ENRR is an environmentally friendly and safe technology in considering of the using water/air as sustainable precursors, and the utilization of renewable electricity as power source [14–19]. Unfortunately, ENRR currently suffers from a poor efficiency of NH_3 production, where nitrogen adsorption and activation at electrocatalyst surface are two key bottlenecks [20–22]. To address these problems, it is urgent to search for effective strategies of improving the activity of ENRR electrocatalysts.

Recently, electric field effect has been used to promote the activity and selectivity of electrocatalysts [23–31]. An engineered electric field can not only significantly alter the charge distribution of metal active sites of catalysts, but also effectively affect the adsorbing behaviors of reactants and intermediates [32,33]. For instance, Sargent et al. firstly engineered a local electric field at Au electrocatalyst to enhance the polarization of CO_2 molecules for electrochemical reduction [34]. Lu et al. found that an introduced built-in electric field at the interface of TiO_2/CuCl can accumulate NO_3^- ions, which significantly promotes the electrocatalytic nitrate reduction reaction (NO_3RR) performance [29]. Furthermore, Dauenhauer and workers reported that local electric field could remarkably tune the adsorption energies of HCOOH molecules on the Pt (111) surface, thus altering reaction pathways of formic acid oxidation [35]. Additionally, Zhang et al. revealed that a polarized electric field of tourmaline nanoparticles (TNPs) facilitates electron transport for formic acid oxidation [36]. Although electric field effect has been impressively reported in these catalysis systems, we noted that electric field was mainly used as a powerful driving force to accumulate reactants and regulate the thermodynamic barriers of reactions, which basically ascribed to oriented movement of polar molecule or charged ions driven by electric field. Moreover, in these cases, the engineered electric field largely relies on the shape (i.e. high curvature) or structure (i.e. nanoneedle) of electrodes or electrocatalysts. We observed that electric field effect had been seldomly investigated in ENRR. Different from NO_3^- and HCOOH molecules, N_2 is typical non-polar molecule with

* Corresponding author.
E-mail addresses: bityanyiming@163.com, yanym22@mail.buct.edu.cn (Y.-M. Yan).

https://doi.org/10.1016/j.apcatb.2022.122130
Received 5 September 2022; Received in revised form 9 October 2022; Accepted 28 October 2022
Available online 29 October 2022
0926-3373/© 2022 Elsevier B.V. All rights reserved.

a high centrosymmetric structure (overlap of positive and negative charge centers), which is intrinsically difficult to accumulate N_2 by a local electric field. However, it has been proposed that non-polar molecules can be effectively polarized under an applied electric field [37]. The non-polar molecules can be distorted and polarized through separating its positive/negative charge centers by the repulsion and attraction of opposites charge centers under the engineered electric field. Based on the above analysis, we assumed that constructing an internal electric field on the catalyst should essentially provide a powerful driving force to separate the positive/negative charge centers of non-polar N_2 and efficiently split N≡N triple bonds. To testify this hypothesis, it is imperative to build a rational electrocatalyst model with a modulated interfacial electric field (IEF) for ENRR investigation.

Herein, we demonstrate the construction of an interfacial electric field in CoO-Co_3O_4 heterostructure as an efficient strategy for boosting the ENRR performance. Synchrotron-radiation X-ray absorption fine structure (XAFS) and high-angle annular dark-field scanning transmission electron microscopy (HAADF-STEM) reveal the existence of heterogeneous interfaces during CoO-Co_3O_4. Additionally, we used Zeta potential and Kelvin probe force microscopy (KPFM) to characterize the interfacial electric field engineered by the CoO-Co_3O_4 heterostructure. Moreover, in situ Fourier transform infrared (FTIR) spectra, in situ Raman spectra and Density functional theory (DFT) calculations affirm that accumulated electrons are injected into the empty *p* antibonding orbital of N_2 molecules, enhancing the adsorption of N_2 molecules on electrocatalysts, while the positive/negative charge centers of N_2 molecules are efficiently separated, facilitating the activation of N_2 molecules. This work provides new information of electric field effect in simultaneously boosting N_2 adsorption and activation for ENRR.

2. Experimental section

2.1. Fabrication of CoO, Co_3O_4 and CoO-Co_3O_4

In brief, 0.8 g Co $(CH_3COO)_2$0.4 H_2O, 0.6 g urea, 0.2 g PVP and 0.3 g NaOH were poured into 60 mL ethanol and stirred for 1 h. Then, the above solution was added to a 100 mL Teflon-lined autoclave and calcined at 140 °C for 10 h. We use DI water and ethanol to wash the as-prepared precipitate three times. And it was separated by centrifugation and dried at 60 °C. Finally, the materials were maintained at 250 °C for 1 h in N_2 atmosphere, CoO-Co_3O_4 was prepared. CoO was prepared using the same method, but it was calcined at 300 °C for 1 h in N_2 atmosphere. Similarly, Co_3O_4 was obtained by the same method, but it was calcined at 400 °C for 2 h in air atmosphere.

2.2. Electrochemical experiments

The H-type electrochemical reaction cell was used to measure electrochemical N_2 reduction experiments. The working electrode, counter electrode and reference electrode were the prepared CoO-Co_3O_4/CP electrode, platinum gauze electrode and Ag/AgCl electrode, respectively. N_2 is injected into the 0.1 M Li_2SO_4 electrolyte for 30 min before electrochemistry tests.

2.3. Characterizations and calculations

The details for characterizations and calculations are provided in the supporting information.

3. Results and discussion

3.1. Characterization of the samples

The CoO-Co_3O_4 heterostructure was synthesized by a modified hydrothermal method (see Supporting Information for details). Also, CoO and Co_3O_4 were prepared as control samples. Scanning electron microscopy (SEM) and transmission electron microscope (TEM) were performed to observe the morphology of CoO-Co_3O_4, showing aggregation nanoparticles, as displayed in Figs. S1c and Fig. S2c. For comparison, the images of CoO (Figs. S1a and S2a) and Co_3O_4 nanoparticles were also presented in Figs. S1b and S2b. The particle size distribution was examined based on the TEM images, where the statistical analysis suggests that the average sizes of CoO, Co_3O_4 and CoO-Co_3O_4 are 8.17, 6.05 and 5.93 nm, respectively, in Fig. S2d-f. The high-resolution TEM (HRTEM) images of CoO-Co_3O_4 in Fig. 1a, b show lattice fringes of 0.24 nm and 0.47 nm, ascribing to the (111) (Fig. 1 b1) crystalline plane of CoO and (111) crystalline plane of Co_3O_4 (Fig. 1 b2). Clearly, HRTEM images display abundant and intimate contacting interfaces between CoO and Co_3O_4 components. Meanwhile, HRTEM images of CoO (0.24 nm) and Co_3O_4 (0.47 nm) samples are shown in Fig. S3. In addition, the high-angle annular dark-field scanning transmission electron microscopy (HAADF-STEM) measurement was further performed to investigate the existence of the heterostructure interface in CoO-Co_3O_4. As displayed in Fig. 1c, the HAADF-STEM image reveals the Co atomic arrangements with bright dots and O atomic arrangements with dark dots. Furthermore, we performed FFT of the area marked with pink rectangular in Fig. 1c, in which the light blue and yellow spheres were employed to highlight the ordered Co and O atoms (Fig. 1d). It was observed that Co and O atoms are densely arranged in the upper region, which are assigned to CoO phase, while the looser arrangement parts of Co and O atoms in the under region should be ascribed to Co_3O_4 phase. Again, the apparently observed interface between CoO and Co_3O_4 components in CoO-Co_3O_4 indicates the formation of heterostructure with abundant interface contact. Furthermore, energy-dispersive X-ray spectroscopy (EDS) results indicate that the coexistence of Co and O elements in CoO, Co_3O_4 and CoO-Co_3O_4 heterostructure (Figs. S4, S5 and 1e). The above results definitely prove the successful preparation of CoO-Co_3O_4 and the existence of obvious interface between CoO and Co_3O_4.

Powder X-ray diffraction (PXRD) was conducted to characterize the products (e.g., CoO-Co_3O_4 heterostructure, CoO and Co_3O_4) (Fig. 1f). Clearly, the PXRD of CoO-Co_3O_4 exhibits typical diffraction peaks of CoO (JCPDS No. 65-2902) and Co_3O_4 (JCPDS No. 65-3103), respectively, indicating the successful preparation of CoO-Co_3O_4. XPS was further employed to assess the chemical valence states of CoO, Co_3O_4 and CoO-Co_3O_4 samples. According to the Fig. S6c, the Co 2p spectra of CoO-Co_3O_4 are deconvoluted into a pair of characteristic peaks located at 780.87 eV (Co $2p_{3/2}$) and 795.96 eV (Co $2p_{1/2}$), ascribing to peaks of Co^{2+}; while another pair of strong peaks located at 779.54 eV (Co $2p_{3/2}$) and 794.49 eV (Co $2p_{1/2}$) are attributed to characteristic peaks of Co^{3+}, implying the coexistence of Co^{3+} and Co^{2+}, and two satellite peaks at 804.15 and 788.87 eV [38]. For comparison, the Co 2p spectrum of CoO and Co_3O_4 nanoparticles were also displayed in Fig. S6a and b. Characteristic peaks of Co^{2+} are observed for CoO sample and characteristic peaks of Co^{2+} and Co^{3+} are observed in Co_3O_4 sample. Additionally, two typical peaks of O 1 s for CoO-Co_3O_4 located at 529.62 eV and 531.22 eV, assigning to the lattice oxygen and near absorbed oxygen in Fig. S7c, respectively. The additional peak position at 532.47 eV is attributed to the oxygen species from OH groups in CoO (Fig. S7a) and Co_3O_4 (Fig. S7b) compared with CoO-Co_3O_4[39]. Furthermore, the elemental percentage from XPS is shown in Table S1. To further reveal the oxidation state and the local coordination environment of Co element in CoO-Co_3O_4, X-ray absorption structure (XAS) analysis were carried out. As depicted in Fig. 1g, compared with the normalized Co-edge X-ray absorption near-edge spectroscopy (XANES) of standard Co, CoO and Co_3O_4, we obtained the photon energy of pre-peak (7709.59 eV) of CoO-Co_3O_4, which is located between that of CoO (7708.45 eV) and Co_3O_4 (7710.84 eV). As a result, it indicates the oxidation state of Co species in CoO-Co_3O_4 is between Co^{2+} and Co^{3+} [40]. Besides, we obtained the detailed local coordination chemistry of Co species in CoO-Co_3O_4 from extended XAFS (EXAFS) analysis (Fig. 1h). The EXAFS spectrum of CoO, Co_3O_4 and CoO-Co_3O_4 shows a

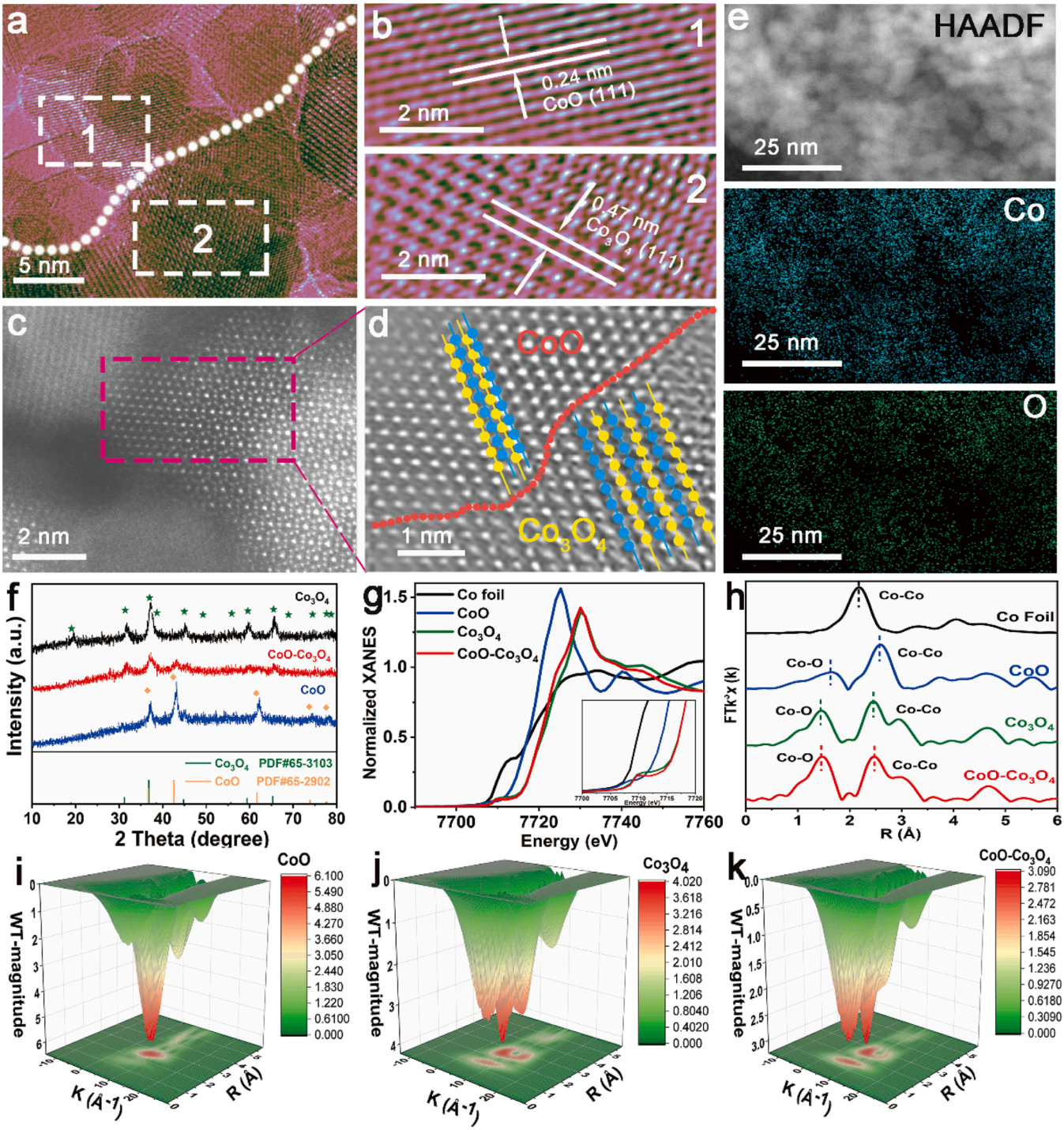

Fig. 1. (a) HRTEM images of CoO-Co_3O_4; (b) Enlarged view of HRTEM images of CoO-Co_3O_4 for the area indicated by white rectangular in (a); (c) HAADF-STEM image of CoO-Co_3O_4; (d) Fast Fourier transform (FFT) patterns of the area indicated by pink rectangular in (c); (e) HAADF and elemental mapping images of CoO-Co_3O_4; (f) XRD of CoO, Co_3O_4 and CoO-Co_3O_4; (g) XANES spectra of Co foil, CoO, Co_3O_4 and CoO-Co_3O_4; (h) EXAFS spectra of Co K-edge of Co foil, CoO, Co_3O_4 and CoO-Co_3O_4; (i-k) WT contour plots of CoO, Co_3O_4 and CoO-Co_3O_4.

strong peak centered at 1.64, 1.44, and 1.45 Å assigned to the Co-O coordination, in comparison with Co foil. Additionally, the peaks located near 2.57, 2.45, and 2.47 Å are well-indexed with Co-Co bond, respectively [41,42]. Moreover, the plots of Wavelet transform (WT) EXAFS of CoO, Co_3O_4 and CoO-Co_3O_4 are displayed in Fig. 1i-k. As depicted by the WT contour plots, CoO-Co_3O_4 exhibits a higher intensity around 1.45 $Å^{-1}$ and 2.47 $Å^{-1}$ relative to that for CoO and Co_3O_4 are ascribed to the Co-Co bonds and Co-O bonds, which are very accord with the EXAFS results[43]. The above results confirm that the CoO-Co_3O_4 was successfully prepared. To confirm the effect of oxygen vacancy in the ENRR application, EPR spectra for three samples were conducted and the results were shown in Fig. S8. Clearly, CoO exhibits stronger EPR signal at the g value of 2.006 than Co_3O_4 and CoO-Co_3O_4, indicating more oxygen vacancy in CoO than the other two samples. However, CoO shows the lowest ENRR activity and selectivity among the three samples. Meanwhile, Co_3O_4 and CoO-Co_3O_4 show similar EPR signal intensity, while the two samples show significantly different ENRR performances. These results unambiguously prove that oxygen vacancy concentration

is not the determined factor of affecting the ENRR performance in our work.

3.2. The electric field analysis of samples

To further characterize the interactions between CoO and Co_3O_4 in the heterostructure, the ultraviolet photoelectron spectra (UPS) was carried out. Fig. S9 shows that the cutoff energy (E_{cutoff}) values of CoO, Co_3O_4 and CoO-Co_3O_4 are 17.33, 16.10 and 16.17 eV, respectively. Furthermore, the equation: $W = hv - |E_{cutoff} - E_f|$ can be used to calculate the work function (WF) [44,45]. As shown in Fig. S9, the WF of individual CoO is 3.61 eV, which is obviously lower than that of the individual Co_3O_4 (5.67 eV). For comparison, the work function of CoO-Co_3O_4 is 5.34 eV, which indicates that the electrons could transfer from CoO to Co_3O_4 phase and a strong interaction between CoO and Co_3O_4 should be existed at the interface. Furthermore, density functional theory (DFT) was carried out to calculate a theoretical WF by subtracting the Fermi level (E_{Fermi}) from the vacuum level (Evac). As displayed in Fig. S10, theoretical WF values for CoO, Co_3O_4, and CoO-Co_3O_4 are 4.65, 5.45, and 4.71 eV, respectively. The theoretical results show that CoO has the smallest WF among all the samples, revealing that electrons can readily escape from the surface of CoO compared to the other two samples, which well match with the UPS measurement results (Fig. S11) [46]. Both the experimental and theoretical results unambiguously testify that the electrons could transfer from CoO phase to Co_3O_4 phase, which consequently results in strong interactions at the interface of CoO and Co_3O_4. In addition, Mott-Schottky measure was employed to investigate the semiconductors type of three samples. As shown in Fig. S12a,b, CoO shows a positive slope plot, and Co_3O_4 displays a negative slope linear region. The phenomena suggests that CoO exhibits a n-type semiconductors feature, while Co_3O_4 shows the p-type nature. Impressively, both positive and negative slopes curves in Mott-Schottky plots of CoO-Co_3O_4 (Fig. S12c) indicate its typical p-n heterostructure feature. Consequently, the electrons should transfer spontaneously from CoO to Co_3O_4 through the heterointerface until their Fermi levels reach equilibrium [47,48]. In addition, the flat potentials for CoO and Co_3O_4 were approximately − 0.53 V and + 0.69 V vs. Ag/AgCl, respectively. Consequently, an interfacial electric field would be generated between CoO and Co_3O_4 in the CoO-Co_3O_4 heterostructure. To clearly illustrate this point, the

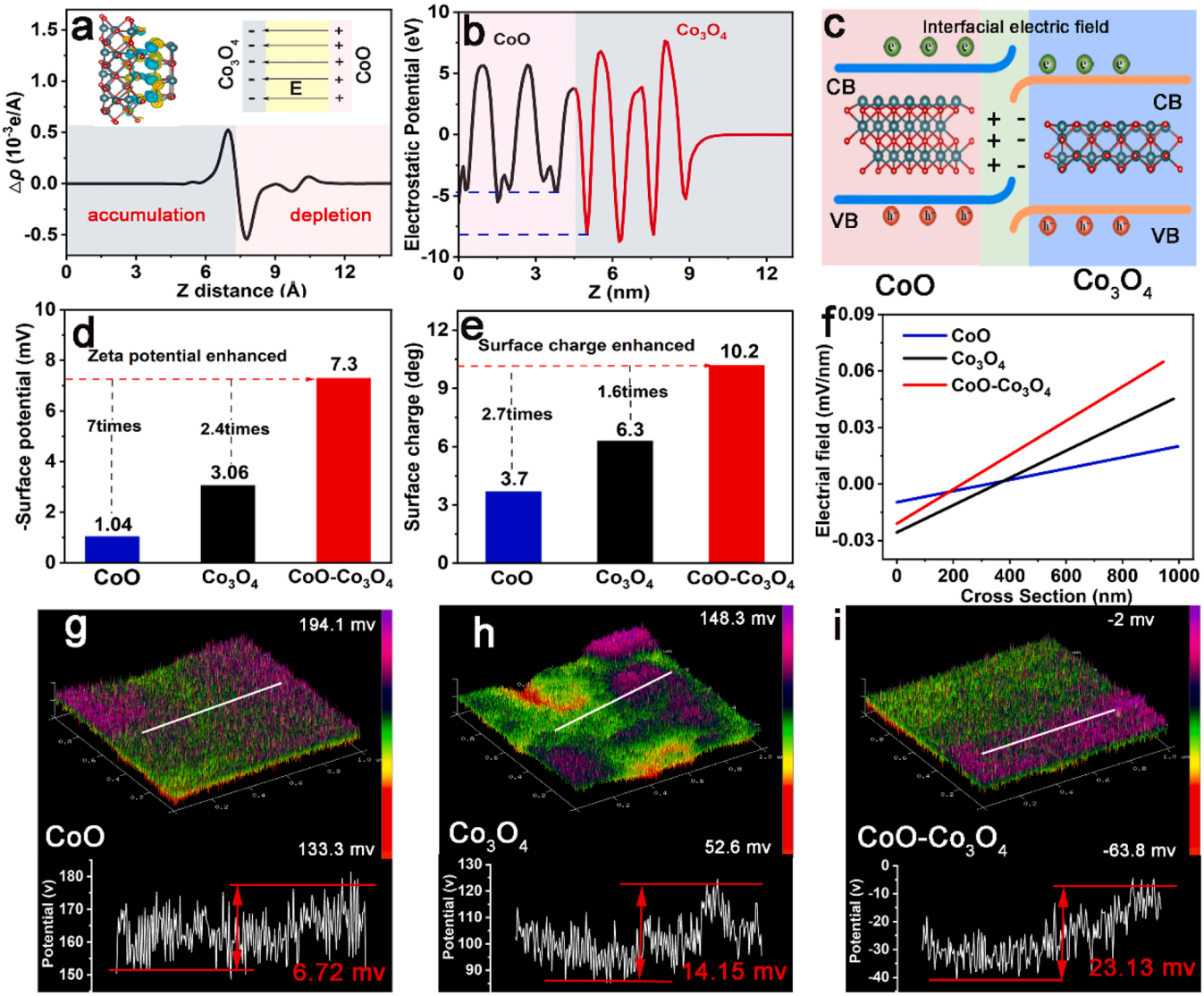

Fig. 2. (a) Plane-averaged charge density difference and its corresponding charge density difference for CoO-Co_3O_4 along z-direction; (b) Electrostatic potential profile of CoO-Co_3O_4; (c) Schematic of interface charge transfer process in the CoO-Co_3O_4 heterostructure; (d) The Zeta potentials of CoO, Co_3O_4 and CoO-Co_3O_4; (e) The surface charge of CoO, Co_3O_4 and CoO-Co_3O_4; (f) The intense distributions of electric field on CoO, Co_3O_4 and CoO-Co_3O_4 surfaces; (g-i) 3D surface potential distribution and corresponding lines canning surface potential profile of CoO, Co_3O_4 and CoO-Co_3O_4.

charge density of CoO-Co_3O_4 slab was computationally calculated to reveal the charge behavior of the interface between CoO and Co_3O_4 phase. As shown in Fig. 2a, the plane-averaged charge density difference of CoO-Co_3O_4 along z-direction was observed, in which the gray and pink regions represent electron accumulation and depletion, respectively. As seen, a substantial charge transfer from CoO to Co_3O_4 was observed in the CoO-Co_3O_4 heterostructure model, resulting in the formation of a strong interfacial electrical field in the heterostructure (inset of Fig. 2a). Additionally, an electron transfer potential (ΔV_{et}=3.69 eV) is obtained between Co_3O_4 (−8.17 eV) region and CoO (−4.68 eV) regions (Fig. 2b and Fig. S13), suggesting that the electrons are prone to transfer from CoO to Co_3O_4 [49]. The computational results are in good accordance with above UPS and Mott-Schottky results. To vividly illustrate the generation of interfacial electric field, Fig. 2c presents the charge transfer process in CoO-Co_3O_4 heterostructure, accompanying with the band bending at the interface of CoO and Co_3O_4 [50]. It is supposed that such an interfacial electric field in CoO-Co_3O_4 heterostructure should favor the electrons accumulation at the interface and benefit the N_2 adsorption and activation.

The Zeta potential of the samples was measured to obtain the surface potential. As depicted in Fig. 2d, the measured Zeta potential of CoO-Co_3O_4 is − 7.30 mV, which is 7 times and 2.4 times higher than that of CoO (−1.04 mV) and Co_3O_4 (−3.06 mV), respectively [51–53]. Furthermore, the electrostatic force microscopy (EFM) was carried out to investigated the distribution of surface charge of electrocatalyst. It is known that EFM is an effective technique to obtain the local electrostatic interaction between the probe and the materials. Fig. S14 displays the EFM images, from which the cross section-deg plot was derived. According to the Fig. 2e, CoO-Co_3O_4 exhibits a remarkable value of 10.20 deg, which is 2.7 times and 1.6 times higher than that of CoO (3.70 deg) and Co_3O_4 (6.30 deg), respectively. As a result, it manifests that the surface charge of CoO-Co_3O_4 is superior to that of CoO and Co_3O_4 [54]. Moreover, Kelvin probe force microscopy (KPFM) was carried out to obtain the surface potential[55,56]. As we all know, KPFM is a method to detect the contact potential difference (CPD) between AFM tip and sample based on a noncontact AFM with high nanoscale spatial resolution. As shown in Fig. 2g-i, the AFM morphology of CoO, Co_3O_4 and CoO-Co_3O_4 were obtained, respectively. Interestingly, we observed that the CPD of CoO-Co_3O_4 is much higher than that of CoO and Co_3O_4, indicating that CoO-Co_3O_4 owns a stronger interfacial electric field. Furthermore, as shown in Fig. S15, the well-fitted surface potentials of three samples exhibit the gradual change of the surface potential, among which CoO-Co_3O_4 (23.13 mV) is much higher than that of individual CoO (6.72 mV) and Co_3O_4 (14.15 mV). The recorded highest surface potential change for CoO-Co_3O_4 should be attributed to the existence of strong interfacial electric field in the heterostructure. In

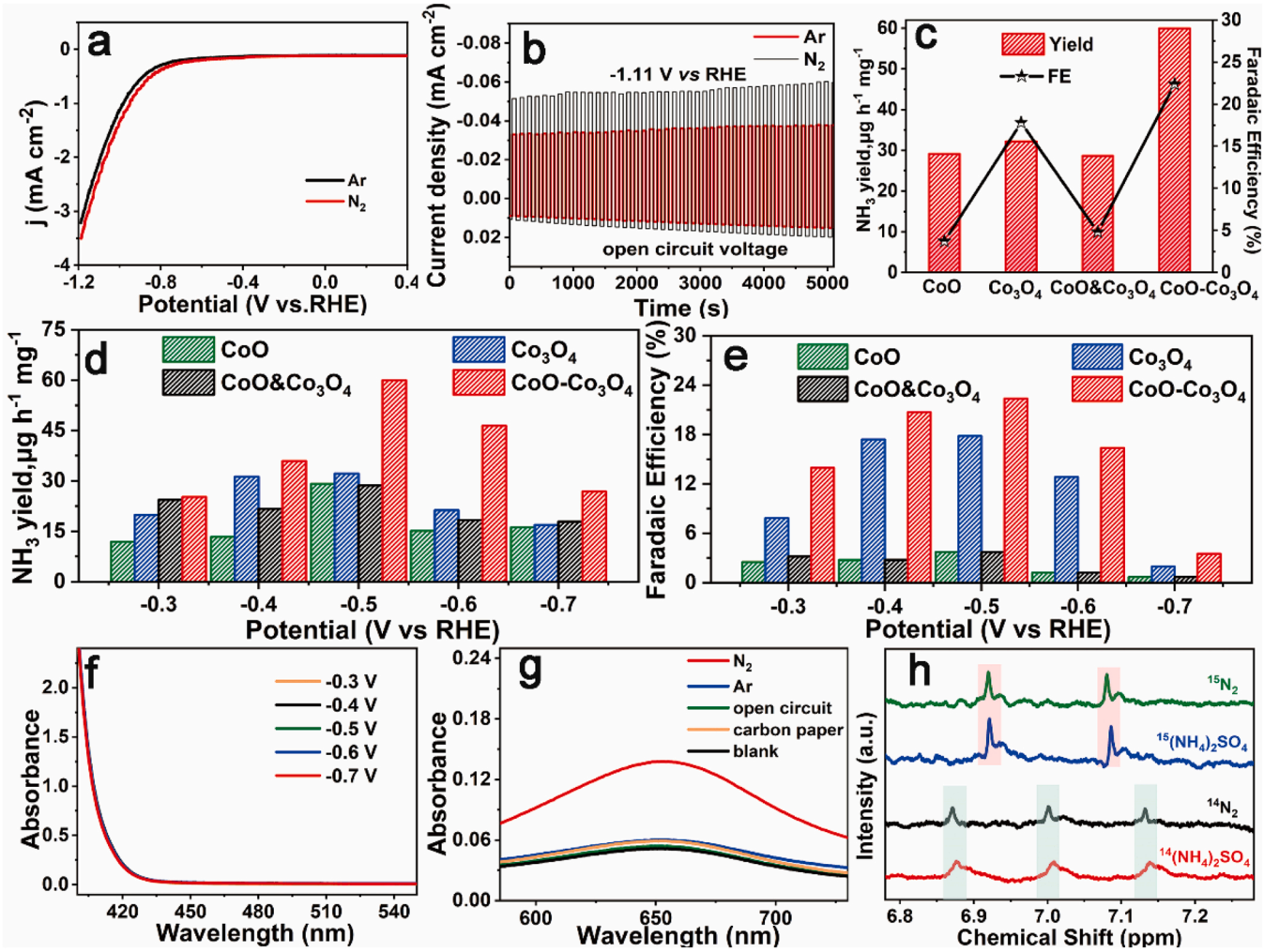

Fig. 3. (a) LSV curves of CoO-Co_3O_4 in Ar- saturated and N_2-saturated 0.1 M Li_2SO_4; (b) Voltage chronoamperometry curves of CoO-Co_3O_4 at − 0.5 V vs RHE and open-circuit potential; (c) NH_3 yield and Faradaic efficiency of CoO, Co_3O_4, CoO&Co_3O_4 and CoO-Co_3O_4 at − 0.5 V vs RHE; (d) NH_3 yield of CoO, Co_3O_4, CoO&Co_3O_4 and CoO-Co_3O_4; (e) Faradaic efficiency of CoO, Co_3O_4, CoO&Co_3O_4 and CoO-Co_3O_4; (f) UV-Vis absorption spectra of the electrolytes estimated by the Watt and Chrisp's method after NRR electrolysis at different potentials; (g) UV–vis absorption spectra at different control conditions; (h) 1 H NMR spectra of CoO-Co_3O_4 fed by $^{14}N_2$ and $^{15}N_2$ gas.

addition, we quantitatively characterized the interfacial electric field intensity by differentiating the fitting surface potentials profile in Fig. S15, as shown in Fig. 2f. Among them, CoO-Co_3O_4 delivers a maximum electric field intensity of 0.07 mV nm^{-1}, which is higher than that of individual CoO (0.02 mV nm^{-1}) and Co_3O_4 (0.05 mV nm^{-1}). The above results convincingly confirm that a strong interfacial electric field has been engineered in the CoO-Co_3O_4 heterostructure. We anticipated that the engineered interfacial electric field in the heterostructure should be beneficial for boosting the ENRR performance of CoO-Co_3O_4 electrocatalyst.

3.3. Electrocatalytic NRR performance of samples

The ENRR performance of the samples was evaluated in 0.1 M Li_2SO_4 electrolyte under ambient conditions (Fig. S16). Linear-sweep voltammetry (LSV) was conducted to roughly investigate the ENRR activity of the as-prepared CoO-Co_3O_4 sample in Ar- or N_2-saturated electrolytes. As displayed in Fig. 3a, the current density of CoO-Co_3O_4 in the N_2-saturated electrolyte is apparently higher than that recorded in Ar atmosphere, implying the occurrence of ENRR over the CoO-Co_3O_4. Simultaneously, the step voltage chronoamperometry experiment was performed to measure the real ENRR current for CoO-Co_3O_4 (Fig. 3b). The recorded currents at − 0.5 V (vs. RHE) are higher than that recorded at open circuit potential. Furthermore, the recorded currents in N_2 are apparently higher than that of in Ar atmosphere. These results manifest that ENRR process has been essentially proceeded at the given voltage for CoO-Co_3O_4. Chronoamperometry was further used to quantitatively assess the ENRR performance of CoO-Co_3O_4. For comparison, we further prepared physically mixed CoO and Co_3O_4 (referred as CoO&Co_3O_4) sample for electrochemical studies. Figs. S19–S22 illustrate the chronoamperometry curves of CoO, Co_3O_4, CoO&Co_3O_4 and CoO-Co_3O_4 at applied potentials from − 0.3 to − 0.7 V vs. RHE, which show no obvious change of current density in 2 h electrolysis. The standard calibrated curves of NH_3 and N_2H_4 are exhibited in Fig. S17 and Fig. S18, respectively. The NH_3 yield is quantitatively determined by the method of indophenol blue and the produced hydrazine (N_2H_4) is estimated by the Watt and Chrisp method utilizing a UV–vis spectrum. As displayed in Fig. 3c and d, the maximum NH_3 yield of CoO-Co_3O_4 is 59.96 μg h^{-1} mg_{cat}^{-1}, which is higher than that of CoO (29.12 μg h^{-1} mg_{cat}^{-1}), Co_3O_4 (32.16 μg h^{-1} mg_{cat}^{-1}) and CoO&Co_3O_4 (28.66 μg h^{-1} mg_{cat}^{-1}). In addition, Fig. 3e shows that the highest FE of CoO-Co_3O_4 is 22.37 %, which is higher than that of CoO (3.7 %), Co_3O_4 (17.8 %) and CoO&Co_3O_4 (4.8 %). In similar conditions, the obtained NH_3 yield and FE of CoO-Co_3O_4 electrocatalyst are superior to those of recently reported ENRR electrocatalysts (Table S2). Fig. 3f shows that no N_2H_4 was detected over CoO-Co_3O_4 electrocatalyst in the range of applied potential, suggesting its high ENRR selectivity. Additionally, we also employed ion chromatograph (IC) to double check the production of ammonia, as shown in Fig. S23. The yield of ammonia for our CoO-Co_3O_4 under optimized condition was calculated as 57.79 μg h^{-1} mg_{cat}^{-1}, which was closely accordance with the colorimetric result (59.96 μg h^{-1} mg_{cat}^{-1}) as depicted in Fig. S23. Again, the IC results confirmed the reliability of the ammonia detection by spectrophotometry. In addition, we investigated the stability of CoO-Co_3O_4 electrocatalyst, as shown in Fig. S24. It was observed that NH_3 yield rate and FE for CoO-Co_3O_4 electrocatalyst only show a slight decrease during five continuous cycles (each cycle lasts two hours) at an applied potential of − 0.5 V in N_2-saturated electrolytes, implying the excellent stability of CoO-Co_3O_4 electrocatalyst. Furthermore, the XRD and HRTEM were performed to verify the structure stability, and the results were provided in Fig. S25. Clearly, the diffraction peaks of XRD and lattice fringe for CoO-Co_3O_4 show no obvious change after the long-time operation, indicating the good stability of CoO-Co_3O_4.

Several control experiments were conducted to confirm the origin of the produced NH_3. According to the Fig. 3g, no NH_3 was detected in all control tests (2 h electrolysis in Ar-saturated electrolytes, on carbon paper, no electrolysis in N_2-saturated electrolyte and open circuit potential). Moreover, the nuclear magnetic resonance (NMR) was also conducted to trace the origin of the produced NH_3. According to Fig. 3h, a distinct triplet peaks for $^{14}NH_4^+$ was recorded by 1 H nuclear magnetic resonance (NMR) tests upon using $^{14}N_2$ as a feeding gas. In contrast, the 1 H NMR spectra of $^{15}N_2$ exhibits two peaks for $^{15}NH_4^+$ using $^{15}N_2$ as a feeding gas in the same ENRR experiment. These experiment results unambiguously demonstrate that the produced NH_3 convincedly arises from the ENRR rather than any nitrogen contaminants. Moreover, the Brunauer-Emmett-Teller (BET) surface area was detected to be 100.58 m^2 g^{-1} for CoO-Co_3O_4, which is larger than that of CoO (71.67 m^2 g^{-1}) and Co_3O_4 (94.78 m^2 g^{-1}) according to Fig. S26. It is known that large surface area of CoO-Co_3O_4 should be beneficial for exposing more active sites and boosting the performance of ENRR. In considering of this, we normalized the NH_3 yield of three samples with BET, as shown in Fig. S27, respectively. The normalized NH_3 yield of CoO-Co_3O_4 is 0.596 mg h^{-1} m_{SBET}^{-2}, which is still higher than that of CoO (0.339 mg h^{-1} m_{SBET}^{-2}) and Co_3O_4 (0.406 mg h^{-1} m_{SBET}^{-2}). As such, it suggests that the significant ENRR performance obtained with CoO-Co_3O_4 should be ascribed to its unique heterostructure, as well as the engineered interfacial electric field. The electrochemically active surface area (ECSA) of the samples was further measured. As shown in Fig. S28, CoO-Co_3O_4 had a smallest capacitance of 0.0232 μF cm^{-2} than that of CoO (0.0446 μF cm^{-2}) and Co_3O_4 (0.0543 μF cm^{-2}), implying that the former had smaller ECSA with fewer activity sites. However, the obtained NH_3 yield of CoO-Co_3O_4 electrocatalyst is superior to that of other samples. Above results firmly demonstrate the crucial role of interfacial electric field in the ENRR. Furthermore, the electrochemical impedance spectroscopy (EIS) experiment was carried to evaluate the charge transfer behavior in Fig. S29. In addition, the fitted equivalent circuit was also provided as an inset in Fig. S29, from which the Rct values for CoO-Co3O4 was 232.3 Ω. It is much lower than the Rct of the CoO (726.2 Ω) and Co3O4 (448.4 Ω), indicating better electron-transport characteristics.

3.4. Activity enhancement mechanism of CoO-Co_3O_4

To investigate the intrinsic reason of the high electrocatalytic performance of CoO-Co_3O_4 heterostructure, N_2 temperature-programmed desorption (N_2-TPD) was carried out. As shown in Fig. 4a, the profile of N_2-TPD for CoO-Co_3O_4 exhibits a characteristic peak located at approximately 293 ℃, ascribing to the chemisorption of nitrogen [57, 58]. Furthermore, the N_2-TPD profiles of CoO and Co_3O_4 display chemical desorption peaks located at 277 ℃ and 269 ℃, respectively, which both are negative than that of CoO-Co_3O_4 heterostructure. It implies that CoO-Co_3O_4 possesses stronger N_2 absorption ability than that of CoO and Co_3O_4. Furthermore, in situ Raman measurement was conducted within different time ranges from 0 to 60 min at − 0.5 V to explore the possible reaction intermediates, as well as to investigate the N_2 adsorption and activation ability. As shown in Fig. 4b, for CoO-Co_3O_4 sample, we observed a strong characteristic peak located at 190 cm^{-1}, assigning to Co-N bond. Fig. S30 shows that Co-N peak of CoO-Co_3O_4 is significantly stronger than that of CoO and Co_3O_4. It suggests that N_2 molecules are tend to adsorb more strongly on CoO-Co_3O_4 electrocatalyst than other two samples. Another characteristic peak appeared at 528 cm^{-1} is assigned to the stretching modes of N-N species. Again, the stretching mode of N-N species recorded with CoO-Co_3O_4 is stronger than that recorded with CoO and Co_3O_4, implying that N_2 molecules should be strongly polarized at CoO-Co_3O_4 electrocatalyst in the presence of interfacial electric field [59]. In addition, in situ Fourier transform infrared (FTIR) spectroscopy was applied to dynamically trace the reaction process over the samples. As shown in Fig. 4c-e, we observed a peak at 1382 cm^{-1} indexed as N-N stretching vibration at CoO-Co_3O_4 surface. For comparison, the N-N stretching vibration peak was observed at 1397 cm^{-1} for CoO and 1391 $cm^{-1}$for Co_3O_4, respectively. Consequently, the obvious blueshift of N-N stretching vibration peak observed

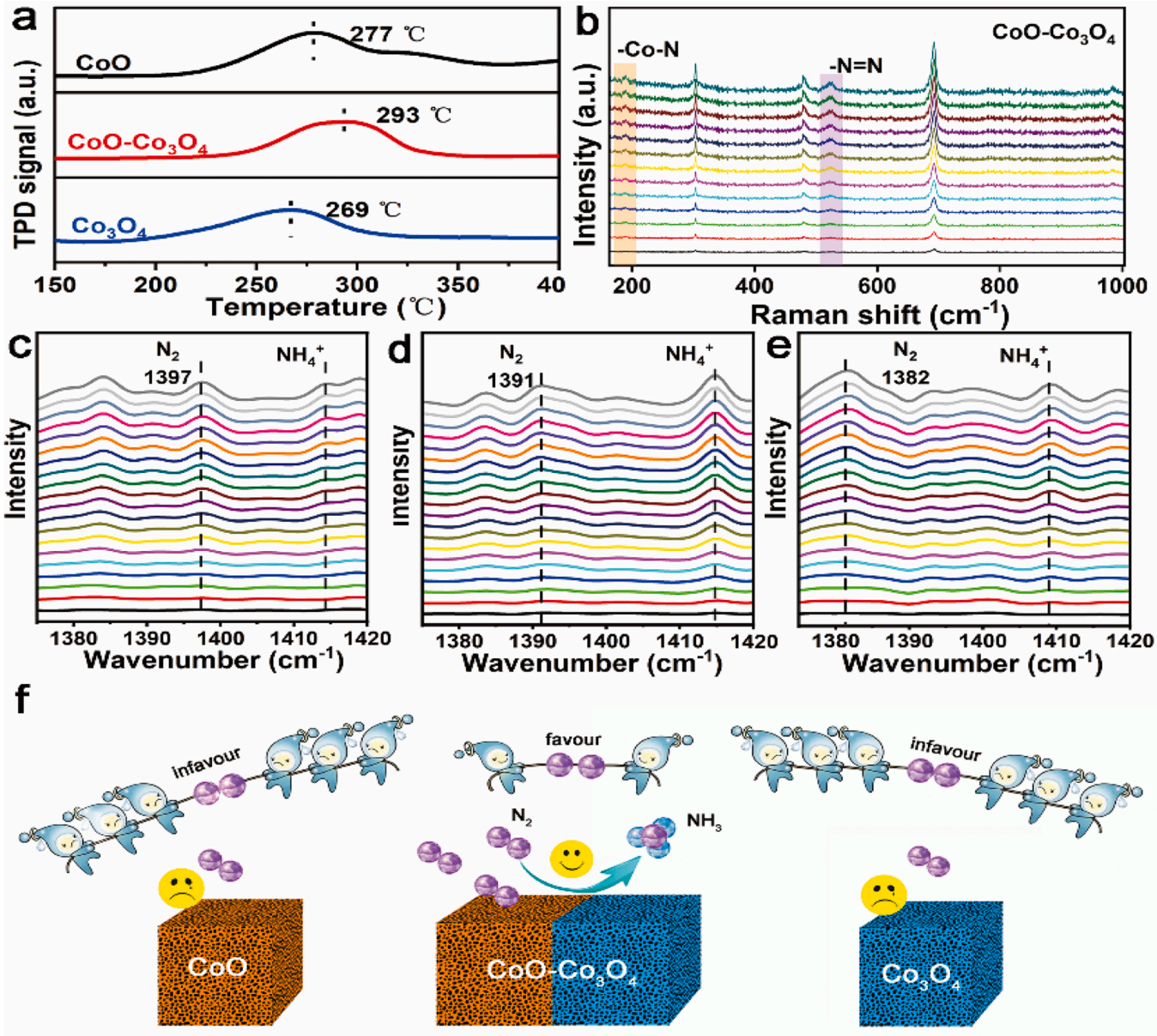

Fig. 4. (a) N_2-TPD profiles for the CoO, Co_3O_4 and CoO-Co_3O_4; (b) In situ Raman spectrum of the CoO-Co_3O_4 at − 0.5 V in 0.1 M Li_2SO_4; (c-e) In situ FTIR spectra of CoO (left), Co_3O_4 (middle) and CoO-Co_3O_4 (right); (f) Schematic diagram showing that interfacial electric field engineered in CoO-Co_3O_4 heterostructure enhances N_2 adsorption and activation during ENRR.

at CoO-Co_3O_4 strongly suggests that N≡N bond was efficiently enlarged when N_2 molecule was adsorbed on CoO-Co_3O_4 [60,61]. Noted that the peak located at 1409 cm^{-1} is the signal of NH_4^+ intermediate detected at CoO-Co_3O_4 sample [62]. Above all, these experimental results demonstrate that N_2 could be more efficiently absorbed and the N≡N bond can be more effectively activated on CoO-Co_3O_4 electrocatalyst, which both are greatly contributed to enhancing the ENRR performance. We assumed that the engineered interfacial electric field plays a crucial role in accelerating the ENRR process at CoO-Co_3O_4. To elucidate the role of interfacial electric field in the catalysis system, Fig. 4f presents a cartoon picture depicting the ENRR occurred at CoO, Co_3O_4 and CoO-Co_3O_4 electrocatalysts. Compared with CoO and Co_3O_4, CoO-Co_3O_4 generates a strong interfacial electric field at the phase interface of heterostructure. Correspondingly, the interfacial electric field boosts the adsorption and activation of N_2, which are prerequisite steps of ENRR process.

The density functional theory (DFT) calculations were performed to further investigate the relationship between the unique structure of CoO-Co_3O_4 electrocatalyst and its excellent ENRR performance. Fig. S31 shows the built model structures of CoO, Co_3O_4 and CoO-Co_3O_4. To gain insights into the effect of interfacial electric field on N_2 adsorption and activation, we calculated the geometrical structures of N_2 adsorbed on the samples. As displayed in Fig. 5a, the calculated bond lengths of Co-N are 1.813 Å, 1.817 Å and 1.797 Å, for CoO, Co_3O_4 and CoO-Co_3O_4, respectively. The smallest bond length of Co-N obtained for CoO-Co_3O_4 implies the strongest N_2 binding affinity of CoO-Co_3O_4. Similarly, the adsorption free energies of N_2 are − 1.47 eV, − 0.97 eV and − 5.48 eV for CoO, Co_3O_4 and CoO-Co_3O_4, which further verifies the higher N_2 adsorption ability of CoO-Co_3O_4 than other samples. Particularly, the N≡N bond lengths of adsorbed N_2 on CoO, Co_3O_4 and CoO-Co_3O_4 are 1.102 Å, 1.125 Å and 1.128 Å, respectively. These values are clearly larger than that of a free N_2 molecule (1.100 Å), indicating that the N≡N bond should be elongated in the adsorbed state at the surface of electrocatalysts. Notably, CoO-Co_3O_4 exhibits a stronger capacity of elongating the N≡N bond than other samples, which should be

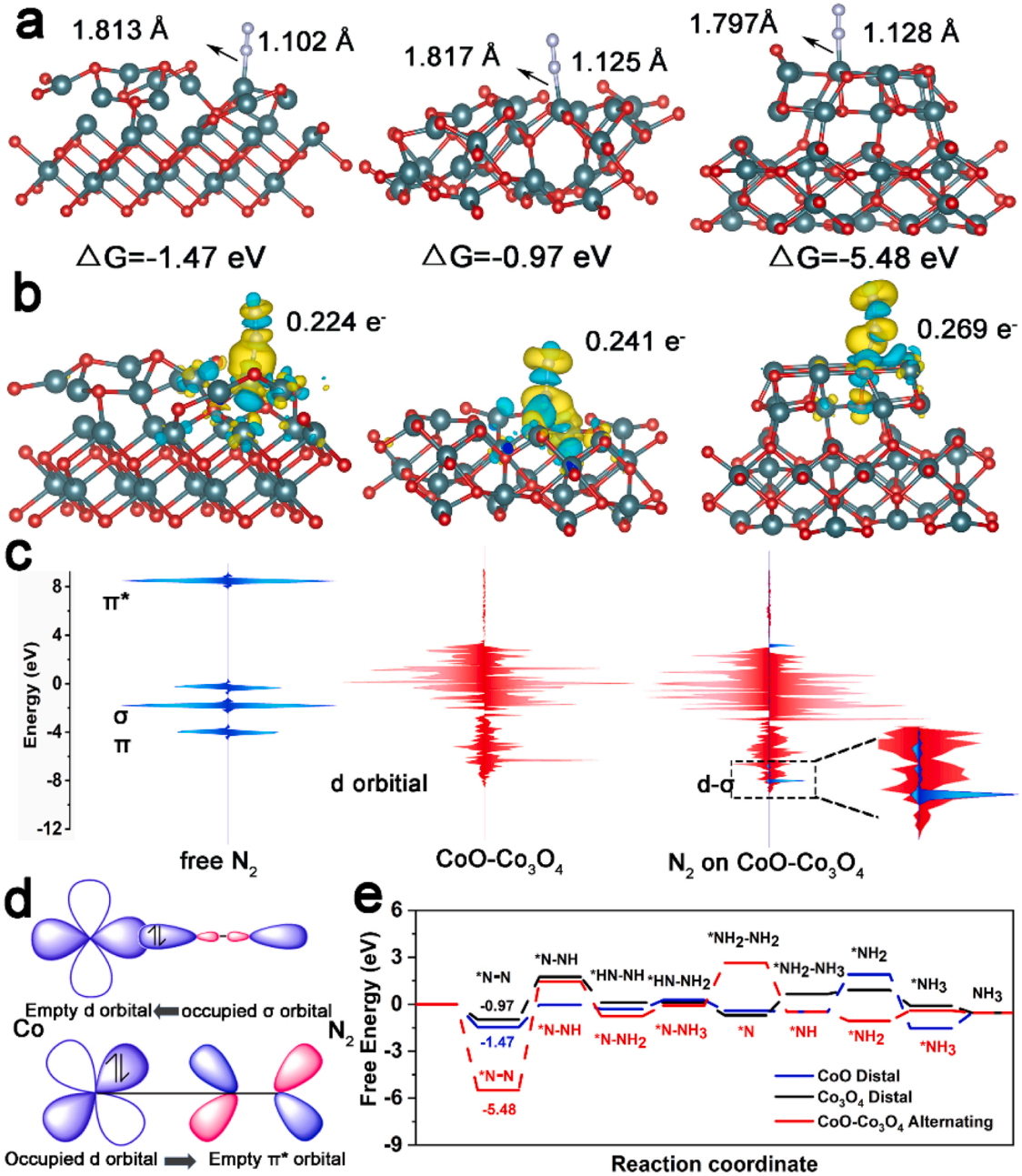

Fig. 5. (a) Structures of N_2 adsorbed on CoO (left), Co_3O_4 (middle) and CoO-Co_3O_4 (right) and the adsorption free energy ΔG; (b) Corresponding charge density and the charge transfer values from Co to N_2; (c) The PDOS for free N_2; PDOS of CoO-Co_3O_4 and N_2 molecule adsorbed at CoO-Co_3O_4; (d) Schematic of electron feedback mechanism from *d* orbitals of Co to π^* of N_2 for Co site; (e) Free energy diagram for NRR of CoO, Co_3O_4 and CoO-Co_3O_4.

attributed to its unique interfacial electric field. We supposed that the adsorbed N_2 molecular on CoO-Co_3O_4 is prone to be distorted and polarized under the interfacial electric field. To further understand this interaction, we calculated the charge density difference to elucidate the electron transfer between electrocatalysts and N_2 molecules. As depicted in Fig. 5b, significant electron transfer from Co sites to absorbed N_2 molecule was observed for all samples. The electron transfer numbers calculated on CoO, Co_3O_4 and CoO-Co_3O_4 models are 0.224e^-, 0.241e^- and 0.269e^-, respectively. Again, the enhanced electron transfer from Co site of CoO-Co_3O_4 to adsorbed N_2 molecule could be ascribed to the presence of interfacial electric field in the heterostructure, which is beneficial for the following ENRR process. To elucidate the intrinsic activation mechanism of N_2 molecule, the projected PDOS of free N_2, CoO, Co_3O_4, CoO-Co_3O_4 and the PDOS of N_2 molecule adsorbed at CoO, Co_3O_4 and CoO-Co_3O_4 were calculated for comparisons, as displayed in Fig. 5c and Fig. S32. We observed that the σ orbital of N_2 (blue line) can essentially overlap the *d* orbital of Co site of the samples, indicating a favorable orbital hybridization between N_2 and electrocatalysts. Especially, for N_2 molecule adsorbed on CoO-Co_3O_4, the intensity of σ-*d* orbital hybridization is much stronger than that observed with other samples, implying a much stronger interaction between N_2 and the Co site of CoO-Co_3O_4. Such a stronger interaction suggests that N≡N bond of N_2 molecule adsorbed on CoO-Co_3O_4 surface could be more easily polarized and the following ENRR process could be more easily ignited. Fig. 5d presents a schematic picture to illustrate the "acceptance-donation" mechanism. Co atom with empty *d* orbitals can accept lone-pair electrons of N_2, while the partially filled *d* orbital donates electrons back to the antibonding π^* orbital of the adsorbed N_2 molecule (π

backdonation), forming an "acceptance-donation" route for the electron transfer to weak the N≡N bond and activate N_2 molecule. To clarify the effect of interfacial electric field on the ENRR performance of CoO-Co_3O_4 electrocatalyst, the N_2 electroreduction free energy of CoO, Co_3O_4 and CoO-Co_3O_4 was calculated for comparison (Fig. 5e). Noted that the optimized configurations of the adsorbed *N-N, *N-NH, *N-NH_2, *HN-NH and other intermediates on CoO, Co_3O_4 and CoO-Co_3O_4 are presented in Figs. S33–S35, respectively. The ENRR on CoO, Co_3O_4 and CoO-Co_3O_4 follows the distal, distal and alternating pathway, respectively. Apparently, the free energy diagrams of N_2 reduction on the samples show that the adsorption of N_2 on the electrocatalysts is the rate determined step (RDS) of the ENRR. For comparison, the adsorption free energy (ΔG) of RDS on CoO-Co_3O_4 is − 5.48 eV, which is much lower than that of CoO (−1.47 eV) and Co_3O_4 (−0.97 eV), suggesting that N_2 is prone to be readily adsorbed and activated on CoO-Co_3O_4. The computational results demonstrate that the CoO-Co_3O_4 heterostructure with a deliberately engineered interfacial electric field favors the adsorption and activation of N_2 on the electrocatalyst surface, which correspondingly enhance the ENRR performance.

4. Conclusion

In conclusion, we have demonstrated the engineering of a strong interfacial electric field in CoO-Co_3O_4 heterostructure as an effective strategy of boosting the ENRR performance. Heterostructure enables electron transfer from CoO phase to Co_3O_4 phase, resulting in an internal electric field at the interface that serves as extra driving force for N_2 capture and activation by efficiently separating the positive/negative charge centers of non-polar N_2. The as-prepared CoO-Co_3O_4 electrocatalyst exhibits a high ENRR catalytic activity, achieving a promising NH_3 yield of 59.96 μg h^{-1} mg_{cat}^{-1} and a high Faradaic efficiency (FE) of 22.37 % in 0.1 M Li_2SO_4. The outstanding activity of CoO-Co_3O_4 is mainly attributed to the existence of interfacial electric field at the CoO-Co_3O_4 interface in the heterostructure, which not only remarkably enhances the N_2 adsorption by forming strong Co-N bonds, but also significantly polarizes the triple N≡N bond by promoting the *σ-d* orbital hybridization. Our findings demonstrate a novel strategy for modulating and triggering the activity of ENRR catalysts, and offer an effective way for sustainable ammonia production.

CRediT authorship contribution statement

Xiaoxuan Wang: Writing – original draft, Data curation, Formal analysis, theoretical calculation. **Xinyue Chi, Zhenzhen Fu, Yuanyuan Xiong, Shuyuan Li, Yebo Yao, Kaixin Zhang, Yongjia Li, Shiyu Wang:** Data collection, analysis and discussion. **Rui Zhao:** Theoretical calculation. **Zhiyu Yang, Yi-Ming Yan:** Data discussion, and draft review & editing.

Declaration of Competing Interest

The authors declare that they have no known competing financial interests or personal relationships that could have appeared to influence the work reported in this paper.

Data availability

No data was used for the research described in the article.

Acknowledgement

Financial support from the National Natural Science Foundation of China (grant nos. 21575016, U20A20154) and from the National Program for Support of Top-notch Young Professionals is gratefully acknowledged.

Appendix A. Supporting information

Supplementary data associated with this article can be found in the online version at doi:10.1016/j.apcatb.2022.122130.

References

[1] G.Y. Zhai, D. Xu, S.N. Zhang, Z.H. Xue, H. Su, Q.Y. Yu, H.H. Wang, X. Lin, Y.X. Lin, L.H. Sun, X.H. Li, J.S. Chen, Isoelectric Si heteroatoms as electron traps for N_2 fixation and activation, Adv. Funct. Mater. 30 (2020) 2005779.
[2] Y. Li, Y.K. Go, H. Ooka, D. He, F. Jin, S.H. Kim, R. Nakamura, Enzyme mimetic active intermediates for nitrate reduction in neutral aqueous media, Angew. Chem. Int Ed. 59 (2020) 9744–9750.
[3] X. Wang, S. Qiu, J. Feng, Y. Tong, F. Zhou, Q. Li, L. Song, S. Chen, K.H. Wu, P. Su, S. Ye, F. Hou, S.X. Dou, H.K. Liu, G.Q. Max Lu, C. Sun, J. Liu, J. Liang, Confined Fe-Cu clusters as sub-nanometer reactors for efficiently regulating the electrochemical nitrogen reduction reaction, Adv. Mater. 32 (2020) 2004382.
[4] T. Wu, X. Zhu, Z. Xing, S. Mou, C. Li, Y. Qiao, Q. Liu, Y. Luo, X. Shi, Y. Zhang, X. Sun, Greatly improving electrochemical N_2 reduction over TiO_2 nanoparticles by Iron doping, Angew. Chem. Int Ed. 58 (2019) 18449–18453.
[5] H. Fei, T. Guo, Y. Xin, L. Wang, R. Liu, D. Wang, F. Liu, Z. Wu, Sulfur vacancy engineering of MoS_2 via phosphorus incorporation for improved electrocatalytic N_2 reduction to NH_3, Appl. Catal. B 300 (2022), 120733.
[6] M.L. Yuan, J.W. Chen, Y.L. Bai, Z.J. Liu, J.X. Zhang, T.K. Zhao, Q. Wang, S.W. Li, H. Y. He, G.J. Zhang, Unveiling electrochemical urea synthesis by Co-activation of CO_2 and N_2 with mott-schottky heterostructure catalysts, Angew. Chem. Int Ed. 60 (2021) 10910–10918.
[7] M.L. Yuan, H.H. Zhang, Y. Xu, R.J. Liu, R. Wang, T.K. Zhao, J.X. Zhang, Z.J. Liu, H. Y. He, C. Yang, S.J. Zhang, G.J. Zhang, Artificial frustrated Lewis pairs facilitating the electrochemical N_2 and CO_2 conversion to urea, Chem. Catal. 2 (2022) 309–320.
[8] M. Kim, H. Nam, J. Choi, H.S. Kim, H.W. Lee, D. Kim, J. Kong, S.S. Han, S.Y. Lee, H. S. Park, Hydrogen bonding-mediated enhancement of bioinspired electrochemical nitrogen reduction on $Cu_{2-x}S$ catalysts, ACS Catal. 10 (2020) 10577–10584.
[9] M. Nazemi, P. Ou, A. Alabbady, L. Soule, A. Liu, J. Song, T.A. Sulchek, M. Liu, M. A. El-Sayed, Electrosynthesis of ammonia using porous bimetallic Pd–Ag nanocatalysts in Liquid- and gas-phase systems, ACS Catal. 10 (2020) 10197–10206.
[10] Y. Wen, H. Zhu, J. Hao, S. Lu, W. Zong, F. Lai, P. Ma, W. Dong, T. Liu, M. Du, Metal-free boron and sulphur co-doped carbon nanofibers with optimized p-band centers for highly efficient nitrogen electroreduction to ammonia, Appl. Catal. B 292 (2021), 120144.
[11] M.L. Yuan, J.W. Chen, Y. Xu, R.J. Liu, T.K. Zhao, J.X. Zhang, Z.Y. Ren, Z.J. Liu, C. Streb, H.Y. He, C. Yang, S.J. Zhang, G.J. Zhang, Highly selective electroreduction of N_2 and CO_2 to urea over artificial frustrated Lewis pairs, Energy Environ. Sci. 14 (2021) 6605–6615.
[12] M.L. Yuan, J.W. Chen, Y.L. Bai, Z.J. Liu, J.X. Zhang, T.K. Zhao, Q.N. Shi, S.W. Li, X. Wang, G.J. Zhang, Electrochemical C-N coupling with perovskite hybrids toward efficient urea synthesis, Chem. Sci. 12 (2021) 6048–6058.
[13] Y.X. Liu, H.H. Wang, T.J. Zhao, B. Zhang, H. Su, Z.H. Xue, X.H. Li, J.S. Chen, Schottky barrier induced coupled interface of electron-rich N-doped carbon and electron-deficient Cu: in-built lewis acid-base pairs for highly efficient CO_2 fixation, J. Am. Chem. Soc. 141 (2019) 38–41.
[14] C. Yang, B. Huang, S. Bai, Y. Feng, Q. Shao, X. Huang, A generalized surface chalcogenation strategy for boosting the electrochemical N_2 fixation of metal nanocrystals, Adv. Mater. 32 (2020) 2001267.
[15] Y. Yang, L. Zhang, Z. Hu, Y. Zheng, C. Tang, P. Chen, R. Wang, K. Qiu, J. Mao, T. Ling, S.Z. Qiao, The crucial role of charge accumulation and spin polarization in activating carbon-based catalysts for electrocatalytic nitrogen reduction, Angew. Chem. Int Ed. 59 (2020) 4525–4531.
[16] Y. Yao, S. Zhu, H. Wang, H. Li, M. Shao, A spectroscopic study of electrochemical nitrogen and nitrate reduction on rhodium surfaces, Angew. Chem. Int. Ed. 59 (2020) 10479–10483.
[17] L. Zhang, M. Cong, X. Ding, Y. Jin, F. Xu, Y. Wang, L. Chen, L. Zhang, A janus Fe-SnO2 catalyst that enables bifunctional electrochemical nitrogen fixation, Angew. Chem. Int. Ed. 59 (2020) 10888–10893.
[18] M.L. Yuan, J.W. Chen, H.H. Zhang, Q.G. Li, L. Zhou, C. Yang, R.J. Liu, Z.J. Liu, S. J. Zhang, G.J. Zhang, Host–guest molecular interaction promoted urea electrosynthesis over a precisely designed conductive metal–organic framework, Energy Environ. Sci. 15 (2022) 2084–2095.
[19] Y.X. Lin, S.N. Zhang, Z.H. Xue, J.J. Zhang, H. Su, T.J. Zhao, G.Y. Zhai, X.H. Li, M. Antonietti, J.S. Chen, Boosting selective nitrogen reduction to ammonia on electron-deficient copper nanoparticles, Nat. Commun. 10 (2019) 4380.
[20] G. Lin, Q. Ju, X. Guo, W. Zhao, S. Adimi, J. Ye, Q. Bi, J. Wang, M. Yang, F. Huang, Intrinsic electron localization of metastable MoS_2 boosts electrocatalytic nitrogen reduction to ammonia, Adv. Mater. 33 (2021) 2007509.
[21] G. Fan, W. Xu, J. Li, J.L. Chen, M. Yu, Y. Ni, S. Zhu, X.C. Su, F. Cheng, Nanoporous NiSb to enhance nitrogen electroreduction via tailoring competitive adsorption sites, Adv. Mater. 33 (2021) 2101126.
[22] K. Ba, G. Wang, T. Ye, X. Wang, Y. Sun, H. Liu, A. Hu, Z. Li, Z. Sun, Single faceted two-dimensional Mo_2C electrocatalyst for highly efficient nitrogen fixation, ACS Catal. 10 (2020) 7864–7870.
[23] B. Yang, K. Liu, H. Li, C. Liu, J. Fu, H. Li, J.E. Huang, P. Ou, T. Alkayyali, C. Cai, Y. Duan, H. Liu, P. An, N. Zhang, W. Li, X. Qiu, C. Jia, J. Hu, L. Chai, Z. Lin, Y. Gao,

M. Miyauchi, E. Cortes, S.A. Maier, M. Liu, Accelerating CO_2 electroreduction to multicarbon products via synergistic electric-thermal field on copper nanoneedles, J. Am. Chem. Soc. 144 (2022) 3039–3049.
[24] L.D. Chen, M. Urushihara, K. Chan, J.K. Nørskov, Electric field effects in electrochemical CO_2 reduction, ACS Catal. 6 (2016) 7133–7139.
[25] F. Che, J.T. Gray, S. Ha, N. Kruse, S.L. Scott, J.-S. McEwen, Elucidating the roles of electric fields in catalysis: a perspective, ACS Catal. 8 (2018) 5153–5174.
[26] W. Lin, H. Chen, G. Lin, S. Yao, Z. Zhang, J. Qi, M. Jing, W. Song, J. Li, X. Liu, J. Fu, S. Dai, Creating frustrated lewis pairs in defective boron carbon nitride for electrocatalytic nitrogen reduction to ammonia, Angew. Chem. Int Ed. 61 (2022), e202207807.
[27] A. Nairan, C. Liang, S.-W. Chiang, Y. Wu, P. Zou, U. Khan, W. Liu, F. Kang, S. Guo, J. Wu, C. Yang, Proton selective adsorption on Pt–Ni nano-thorn array electrodes for superior hydrogen evolution activity, Energy Environ. Sci. 14 (2021) 1594–1601.
[28] F.Y. Gao, S.J. Hu, X.L. Zhang, Y.R. Zheng, H.J. Wang, Z.Z. Niu, P.P. Yang, R.C. Bao, T. Ma, Z. Dang, Y. Guan, X.S. Zheng, X. Zheng, J.F. Zhu, M.R. Gao, S.H. Yu, High-curvature transition-metal chalcogenide nanostructures with a pronounced proximity effect enable fast and selective CO_2 electroreduction, Angew. Chem. Int. Ed. 59 (2020) 8706–8712.
[29] W.J. Sun, H.Q. Ji, L.X. Li, H.Y. Zhang, Z.K. Wang, J.H. He, J.M. Lu, Built-in electric field triggered interfacial accumulation effect for efficient nitrate removal at ultra-low concentration and electroreduction to ammonia, Angew. Chem. Int Ed. 60 (2021) 22933–22939.
[30] S.N. Zhang, P. Gao, L.H. Sun, J.S. Chen, X.H. Li, Tunable surface electric field of electrocatalysts via constructing schottky heterojunctions for selective conversion of trash ions to treasures, Chem. Eur. J. 28 (2022), e202103918.
[31] P. Gao, Z.H. Xue, S.N. Zhang, D. Xu, G.Y. Zhai, Q.Y. Li, J.S. Chen, X.H. Li, Schottky barrier-induced surface electric field boosts universal reduction of NO_x^- in water to ammonia, Angew. Chem. Int. Ed. 60 (2021) 20711–20716.
[32] W.H. Jiandong Yao, Wei Fang, Min Kuang, Ning Jia, Hao Ren, Daobin Liu, C. L. Chade Lv, Jianwei Xu, Qingyu Yan, Promoting electrocatalytic hydrogen evolution reaction and oxygen evolution reaction by fields: effects of electric field, magnetic field, strain, and light, Small Methods 4 (2020) 2000494.
[33] R. Jin, Y. Huang, L. Cheng, H. Lu, D. Jiang, H.-Y. Chen, In situ observation of heterogeneous charge distribution at the electrode unraveling the mechanism of electric field-enhanced electrochemical activity, Chem. Sci. 11 (2020) 4158–4163.
[34] M. Liu, Y. Pang, B. Zhang, P. De Luna, O. Voznyy, J. Xu, X. Zheng, C.T. Dinh, F. Fan, C. Cao, F.P. de Arquer, T.S. Safaei, A. Mepham, A. Klinkova, E. Kumacheva, T. Filleter, D. Sinton, S.O. Kelley, E.H. Sargent, Enhanced electrocatalytic CO_2 reduction via field-induced reagent concentration, Nature 537 (2016) 382–386.
[35] M. Shetty, M.A. Ardagh, Y. Pang, O.A. Abdelrahman, P.J. Dauenhauer, Electric-field-assisted modulation of surface thermochemistry, ACS Catal. 10 (2020) 12867–12880.
[36] G. Luo, S. Hu, D. Niu, S. Sun, X. Zhang, Well-designed internal electric field from nano-ferroelectrics promotes formic acid oxidation on Pd, Nanoscale 14 (2022) 6007–6020.
[37] E.A. Moelwyn-Hughes, Physical Chemistry (1957) 373.
[38] J. Bae, D. Shin, H. Jeong, B.-S. Kim, J.W. Han, H. Lee, Highly water-resistant La-doped Co_3O_4 catalyst for CO oxidation, ACS Catal. 9 (2019) 10093–10100.
[39] Y.Z. Qian Zhao, Chunfeng Song, Qingling Liua, Na Jia, Degang Ma, X. Lu, Novel monolithic catalysts derived from in-situ decoration of Co_3O_4 and hierarchical Co_3O_4@MnOx on Ni foam for VOC oxidation, Appl. Catal. B 265 (2020), 118552.
[40] J. Wang, R. Gao, L. Zheng, Z. Chen, Z. Wu, L. Sun, Z. Hu, X. Liu, CoO/CoP heterostructured nanosheets with an O–P interpenetrated interface as a bifunctional electrocatalyst for Na–O_2 battery, ACS Catal. 8 (2018) 8953–8960.
[41] Z. Xiao, Y. Wang, Y.-C. Huang, Z. Wei, C.-L. Dong, J. Ma, S. Shen, Y. Li, S. Wang, Filling the oxygen vacancies in $Co_3O_4$with phosphorus: an ultra-efficient electrocatalyst for overall water splitting, Energy Environ. Sci. 10 (2017) 2563–2569.
[42] Q. Zhang, P. Yang, H. Zhang, J. Zhao, H. Shi, Y. Huang, H. Yang, Oxygen vacancies in Co_3O_4 promote CO_2 photoreduction, Appl. Catal. B 300 (2022), 120729.
[43] Y. Lu, T. Liu, C.L. Dong, Y.C. Huang, Y. Li, J. Chen, Y. Zou, S. Wang, Tuning the selective adsorption site of biomass on Co_3O_4 by Ir single atoms for electrosynthesis, Adv. Mater. 33 (2021) 2007056.
[44] Y. Chen, L. Gong, X. Du, S. Chen, W.G. Xie, W.H. Zhang, J. Chen, F.Y. Xie, Comparison of work functions of several materials measured by XPS and UPS, J. Instrum. Anal. 37 (2018) 796–803.
[45] B. Zhang Y.Z. Sun, W.H. Wang, Work function measurements using UPS, Phys. Exam. Test. (2007) 7.
[46] L. Lv, X. He, J. Wang, Y. Ruan, S. Ouyang, H. Yuan, T. Zhang, Charge localization to optimize reactant adsorption on KCu_7S_4/CuO interfacial structure toward selective CO_2 electroreduction, Appl. Catal. B 298 (2021), 120531.
[47] Y. Yang, G. Zeng, D. Huang, C. Zhang, D. He, C. Zhou, W. Wang, W. Xiong, X. Li, B. Li, W. Dong, Y. Zhou, Molecular engineering of polymeric carbon nitride for highly efficient photocatalytic oxytetracycline degradation and H_2O_2 production, Appl. Catal. B 272 (2020), 118970.
[48] J. Qiu, Y. Wang, X. Liu, One-pot hydrothermal synthesis of $CuBi_2O_4$/BiOCl p–n heterojunction with enhanced photocatalytic performance for the degradation of tetracycline hydrochloride under visible light irradiation, New J. Chem. 46 (2022) 2898–2907.
[49] S. Xue, W. Huang, W. Lin, W. Xing, M. Shen, X. Ye, X. Liang, C. Yang, Y. Hou, Z. Yu, X. Wang, Interfacial engineering of lattice coherency at ZnO-ZnS photocatalytic heterojunctions, Chem. Catal. 2 (2022) 125–139.
[50] J. Jing, J. Yang, W. Li, Z. Wu, Y. Zhu, Construction of interfacial electric field via dual-porphyrin heterostructure boosting Pphotocatalytic hydrogen evolution, Adv. Mater. 34 (2022) 2106807.
[51] J. Yang, J. Jing, W. Li, Y. Zhu, Electron donor-acceptor interface of TPPS/PDI boosting charge transfer for efficient photocatalytic hydrogen evolution, Adv. Sci. 9 (2022), e2201134.
[52] Y. Guo, W. Shi, Y. Zhu, Y. Xu, F. Cui, Enhanced photoactivity and oxidizing ability simultaneously via internal electric field and valence band position by crystal structure of bismuth oxyiodide, Appl. Catal. B 262 (2020), 118262.
[53] C. Cheng, B. He, J. Fan, B. Cheng, S. Cao, J. Yu, An inorganic/organic S-scheme heterojunction H_2 -production photocatalyst and its charge transfer mechanism, Adv. Mater. 33 (2021), e2100317.
[54] P. Ares, T. Cea, M. Holwill, Y.B. Wang, R. Roldan, F. Guinea, D.V. Andreeva, L. Fumagalli, K.S. Novoselov, C.R. Woods, Piezoelectricity in monolayer hexagonal boron nitride, Adv. Mater. 32 (2020) 1905504.
[55] Y. Gao, J. Zhu, H. An, P. Yan, B. Huang, R. Chen, F. Fan, C. Li, Directly probing charge separation at interface of TiO_2 phase junction, J. Phys. Chem. Lett. 8 (2017) 1419–1423.
[56] A. Zhang, R. Zhao, L. Hu, R. Yang, S. Yao, S. Wang, Z. Yang, Y.M. Yan, Adjusting the coordination environment of Mn enhances supercapacitor performance of MnO_2, Adv. Energy Mater. 11 (2021) 2101412.
[57] M. Han, M. Guo, Y. Yun, Y. Xu, H. Sheng, Y. Chen, Y. Du, K. Ni, Y. Zhu, M. Zhu, Effect of heteroatom and charge reconstruction in atomically precise metal nanoclusters on electrochemical synthesis of ammonia, Adv. Funct. Mater. (2022) 2202820.
[58] Q. Meng, Y. Hou, F. Yang, C. Cao, Z. Zou, J. Luo, W. Zhou, Z. Tong, S. Chen, S. Zhou, J. Wang, S. Deng, Modulation of surface properties on cobalt phosphide for high-performance ambient ammonia electrosynthesis, Appl. Catal. B 303 (2022), 120874.
[59] S. Liu, T. Qian, M. Wang, H. Ji, X. Shen, C. Wang, C. Yan, Proton-filtering covalent organic frameworks with superior nitrogen penetration flux promote ambient ammonia synthesis, Nat. Catal. 4 (2021) 322–331.
[60] Z. Zhao, H. Ren, D. Yang, Y. Han, J. Shi, K. An, Y. Chen, Y. Shi, W. Wang, J. Tan, X. Xin, Y. Zhang, Z. Jiang, Boosting nitrogen activation via bimetallic organic frameworks for photocatalytic ammonia synthesis, ACS Catal. 11 (2021) 9986–9995.
[61] Y. Kong, Y. Li, X. Sang, B. Yang, Z. Li, S. Zheng, Q. Zhang, S. Yao, X. Yang, L. Lei, S. Zhou, G. Wu, Y. Hou, Atomically dispersed Zinc(I) active sites to accelerate nitrogen reduction kinetics for ammonia electrosynthesis, Adv. Mater. 34 (2022) 2103548.
[62] Y. Ren, C. Yu, X. Han, X. Tan, Q. Wei, W. Li, Y. Han, L. Yang, J. Qiu, Methanol-mediated electrosynthesis of ammonia, ACS Energy Lett. 6 (2021) 3844–3850.